



# Analyses of Spatial Correlation and Coherence in ABL Flow with a Fleet of UAS

Tamino Wetz<sup>1</sup> · Josef Zink<sup>1</sup> · Jens Bange<sup>2</sup> · Norman Wildmann<sup>1</sup>

Received: 5 September 2022 / Accepted: 14 February 2023  
© The Author(s) 2023

## Abstract

The spatial structures of turbulent flow in the atmospheric boundary layer (ABL) are complex and diverse. Multi-point spatial correlation measurements can help improve our understanding of these structures and their statistics. In this context, we investigate Taylor's hypothesis and the statistics of spatial structures on the microscale. For the first time, simultaneous horizontally distributed wind measurements with a fleet of 20 quadrotor UAS (unmanned aerial systems) are realized. The measurements were taken at different heights and under different atmospheric conditions at the boundary layer field site in Falkenberg of the German Meteorological Service (DWD). A horizontal flight pattern has been specifically developed, consisting of measurements distributed along and lateral to the mean flow direction with separation distances of 5 . . . 205 m. The validity of Taylor's hypothesis is studied by examining the cross-correlations of longitudinally distributed UAS and comparing them with the auto-correlations of single UAS. To assess the similarity of flow structures on different scales, the lateral and longitudinal coherence of the streamwise velocity component is examined. Two modeling approaches for the decay of coherence are compared. The experimental results are in good agreement with the model approaches for neutral atmospheric conditions, whereas in stable and convective ABL, the exponential approaches are not unconditionally valid. The validation results and the agreement with the literature on coherence in the ABL underline the potential of the UAS fleet for the purpose of spatial turbulence measurements.

**Keywords** Coherence · Spatial correlation · Taylor's hypothesis · Turbulence · UAS

---

✉ Tamino Wetz  
[tamino.wetz@dlr.de](mailto:tamino.wetz@dlr.de)

Norman Wildmann  
[norman.wildmann@dlr.de](mailto:norman.wildmann@dlr.de)

<sup>1</sup> Deutsches Zentrum für Luft- und Raumfahrt e.V., Institut für Physik der Atmosphäre, Oberpfaffenhofen, Germany

<sup>2</sup> Center for Applied Geoscience, Eberhard-Karls-Universität Tübingen, Schnarrenbergstr. 94-96, 72076 Tübingen, Germany

# 1 Introduction

The characterization of turbulence is a key aspect of understanding the processes within the atmospheric boundary layer (ABL). The size of turbulent eddies spans a broad range of scales, from millimeters to kilometers - a challenge for experimental research. In order to measure turbulence, various techniques exist in atmospheric science. Most prominently, sonic anemometers allow direct measurement of turbulent fluctuations as point measurements (Rajewski et al. 2013; Mauder and Zeeman 2018). More recently, Doppler wind lidars (DWL) have increasingly been used to derive spatial averages of turbulence parameters (Smalikho et al. 2005; Wildmann et al. 2020). However, for studying spatial structures and their temporal evolution, the techniques are limited in their resolution and rely on assumptions about the state of the atmosphere. To deduce spatial information from point measurements, the frozen turbulence assumption from Taylor is applied (Taylor 1938). This hypothesis states that turbulent eddies remain unchanged in a certain domain or for a certain time and are only advected by the mean wind.

Sonic anemometers and DWL are instruments that can provide long-term observations in the field. For short-term campaigns, airborne in-situ measurements with research aircraft are a way to sample the spatial distribution of turbulence. Within the last two decades, measurements with UAS have become more relevant in ABL research because of their flexible deployment and low cost. For in-situ wind measurements, either fixed-wing (Platis et al. 2018; Wildmann et al. 2015) or rotary-wing UAS—particularly multicopters—are deployed. Multicopters can be equipped with external wind sensors, for example sonic anemometers (Shimura et al. 2018) or hot wire probes (Cuxart et al. 2019). But they can also provide horizontal wind estimates without additional sensors (Neumann and Bartholmai 2015). Fixed-wing UAS have the advantage that larger measurement domains can be studied within the same time period. However, multicopters can be deployed without the necessity of runways or landing strips and can provide stationary measurements at the particular point of interest. A big advantage is that wind measurements can be performed simultaneously at multiple positions when multiple UAS are deployed (Wetz et al. 2021).

Taylor's hypothesis has been tested by various experiments using Doppler wind lidar (Schlipf et al. 2010; Higgins et al. 2012) and arrays of sonic anemometer measurements (e.g., in the HATS field observations, Horst et al. 2004). A fleet of UAS enables additional possibilities with regards to flexibility and simultaneous measurements at multiple points. Mizuno and Panofsky (1975) divided the validity of Taylor's hypothesis into two conditions. First, the similarity within the turbulent flow represented by the coherence along the wind should remain unity, and second, the convection velocity of the eddies should be equal to the local velocity. Particularly the first condition concerning the coherence is analyzed in this study.

For studying turbulent structures, a spanwise array of 10 sonic anemometers was installed at the SLTEST facility in western Utah at a unique site with very low surface roughness over a salt flat. Hutchins and Marusic (2007) examined superstructures (also called very large scale motions), extending over 20 boundary layer depths in length, in high-Reynolds numbers by two-point correlations of laterally distributed, streamwise velocity fluctuation measurements. At the same field site Chauhan et al. (2012) studied the change of the structure's inclination angle under different stability conditions. From a two-point correlation map of vertically separated measurements, an elliptical shape can be derived, with the principal axis representing the structure's inclination angle. The results outline an increasing inclination angle with decreasing stability. Salesky and Anderson (2018) used LES for examining very-large-

scale motions and the modulation of near-wall processes in the convective ABL. The increase in the inclination angle with decreasing stability is confirmed by their studies. Building on that study, Salesky and Anderson (2019) found the size of the large-scale motions remain unchanged while the stability decreases. The turbulence organization in stable stratified ABL has recently been examined by Heisel et al. (2022) in LES. The ramp-up structures, with a positive inclination angle, can also be found in stable conditions.

Besides the correlation of the time series as a whole, the similarity of flow structures at different scales can be studied by the coherence between spatially distributed measurements. Mathematically, the coherence can be described as the normalized cross-spectrum (detailed description found in Sect. 3.4). If the turbulence was frozen, the coherence would be unity for all scales (Panofsky and Mizuno 1975). The coherence can be experimentally studied by at least two spatially separated time series of velocity fluctuations. In the early 1960s, Davenport (1961) first formulated a model of coherence for atmospheric boundary layer flows. He proposed an exponential decay function of the coherence with increasing frequency  $f$  (decreasing eddy size) of the flow structures. The observations are based on vertically separated, streamwise velocity fluctuation measurements. The model predicts an increase of coherence with decreasing separation distances  $\Delta z$  and decreasing mean wind velocity  $\bar{u}$ . For the scaling of the exponential function, a dimensionless decay parameter  $a$  is defined, so that:

$$\gamma_z(f) = e^{-a \frac{\Delta z}{\bar{u}} f}. \quad (1)$$

This model is still widely applied for coherence estimations in the ABL. Pielke and Panofsky (1970) confirmed the exponential characteristic of the coherence from Davenport (1961) by studying the streamwise and lateral wind components for vertically separated measurements. Applying the same decay approach, they found an increase in coherence with decreasing atmospheric stability.

Ropelewski et al. (1973) examined horizontal coherence at different measurement sites, including different horizontal separations and various instrument heights. They stated an increase in the decay parameter by turning from longitudinal to lateral wind directions, including a stronger dependency for the lateral coherence on atmospheric stratification than for the longitudinal coherence. They found that for stable stratification, the lateral decay parameter tends to be larger than for unstable conditions. However, they used different approaches for the lateral and longitudinal decay parameters. In addition to Davenport's formulation, the lateral coherence of streamwise velocity fluctuations includes the ratio of the longitudinal to the lateral integral length scale. This ratio itself is a function of stability (Panofsky 1962).

Schlez and Infield (1998) studied longitudinal and lateral coherence at separation distances of 62 m and larger at 18 m height above ground. They focused only on near neutral stratified atmospheric conditions. In addition to the Davenport formulation, the dependency of turbulence intensity is included for the longitudinal and lateral coherence of the streamwise wind component. The model of the lateral coherence is performed without the normalisation of the lateral separation distance  $\Delta y$  with the mean wind speed  $\bar{u}$ .

Jensen and Kristensen (1979) showed that for isotropic turbulence the lateral coherence does not converge to unity for large scales if the lateral separation  $\Delta y$  exceeds the integral turbulent length scale (ILS) in lateral direction  $L_y$ . Furthermore, they proposed a dependence on the ILS if the separation is not small compared to the length scale, this would lead to a maximum coherence of 0.4 for example for the ratio of  $\Delta y/L_y = 0.5$ . These statements are based on experiments at the Sotra bridge in an altitude of 57 m above water with lateral separations  $\Delta y$  from 5 ... 16 m resulting in a three times lower decay parameter at the bridge

compare to observations over ice in 3 m altitude (Kristensen et al. 1981). Both analyses were limited to neutral stability. They found that the lateral decay parameter is a function of separation distance and altitude, such that the decay parameter  $c_y$  increases with increased ratio of  $\Delta y/z$ .

Knowledge of the coherence in the atmospheric boundary layer is crucial in wind energy science for calculating the aerodynamic loads and further, for estimating the energy production of a wind turbine (WT) (Saranyasoontorn et al. 2004). Therefore, in the Longterm Inflow and Structural Test (LIST) field measurement (Saranyasoontorn et al. 2004) the longitudinal and lateral coherence was studied with multiple anemometers which were laterally separated by 7.7...33 m and vertically separated by 8.5...17 m around a hub height of 23 m. They found an increase in the vertical decay parameter of the streamwise velocity while increasing the vertical distance, based on the original Davenport model. The dependency of the decay parameter on the lateral separation is even greater than on the vertical separation. They also applied a decay model by Thresher et al. (1981) which accounts for the separation distance with an additional term and a scaling parameter in the coherence decay model. Further, comparisons to theoretical models such as the isotropic turbulence model of von Kármán (1948) and the uniform shear turbulence model of Mann (1994) show reasonable agreement with the Mann model, as the von Kármán model generally overestimates the coherence. In the design process of large suspension bridges and large buildings in industrial aerodynamics, the impact of aerodynamic loads by the coherence is considered as well (Midjjiyawa et al. 2021). Cheynet et al. (2016) conducted coherence studies for the structural design of bridges.

Further, the COTUR project studies the offshore turbulence with remote sensing techniques. (Cheynet et al. 2021) measured the lateral coherence using multiple DWL systems with lateral separations of  $\Delta y = 21$  m. Extending the Davenport model by combining the lateral and longitudinal coherence resulted in values about  $c_y = 15 \dots 19$  for the lateral decay parameter.

Simley and Pao (2015) studied the longitudinal coherence of the streamwise wind component in the inflow of a WT using Large Eddy Simulations (LES) and proposed a scan strategy for lidar-based coherence measurements in WT inflow measurements. The time domain is limited to 740 s in their simulation, so that the coherence does not reach unity in every case for the largest resolvable scales. They proposed an approach for the longitudinal coherence which is based on the Davenport model but allows the decay function to converge to smaller values than unity for low frequencies. Furthermore, Mann (1994) evaluates a turbulence model for spatial coherence within different experiments.

In this study, we deploy the SWUF-3D (Simultaneous Wind measurement with Unmanned Flight systems in 3D) fleet of quadrotors to collect distributed wind measurements in the ABL. This approach was validated in a two-week measurement campaign at the boundary layer field site Falkenberg of the German Meteorological Service (DWD) (Wetz et al. 2021). A dedicated measurement pattern is developed for an examination of Taylor's frozen hypothesis theory by studying horizontal correlations between multiple UAS in different atmospheric conditions. Limits of the frozen turbulence assumption are studied with the spatial cross-correlation function of the wind velocity within the UAS-fleet at the field site. The simultaneous UAS measurements enable extensive coherence studies. We specifically focus on the lateral and longitudinal coherence of the streamwise velocity component for various horizontal separation distances between 5 m and 205 m. We analyze the dependency of the coherence on atmospheric stability and the separation distance by studying the applicability of exponential coherence decay models from Davenport (1961) and Schlez and Infield (1998).

In Sect. 2, the experiment, including the measurement systems and the measurement strategies, is shown. Section 3 explains the wind algorithm used within the fleet. Also, methods are introduced for calculating turbulence quantities, boundary layer characteristics, and correlation analysis, including coherence models. In Sect. 4, the results for turbulence measurements and horizontal correlation analyses of the fleet measurements follow. Additionally, the approximation of coherence with different approaches is examined. The results are discussed in Sect. 5 with regard to the limits of the validity of Taylor's frozen hypothesis and the potential of model approaches for coherence at various separation distances and in different atmospheric conditions.

## 2 Experimental Setup

### 2.1 UAS-Fleet

The measurement systems consist of 35 quadrotors of the type Holybro QAV250 with a frame dimension of 0.25 m. Supported by the GNSS and the autopilot, the UAS is able to hover in fixed positions and follow predefined flight paths. The inertial measurement unit (IMU) measures the UAS attitude and its first and second derivatives with a set of sensors, including gyroscopes, accelerometers, and magnetometers. The sensor data are logged to an SD-Card with a temporal resolution between 1 and 250 Hz depending on the sensor type (see also Wildmann and Wetz 2022). With the current system the turbulence can be resolved until 1 Hz (Wetz and Wildmann 2022). Since we do not rely on external wind sensors, the disturbance of the rotors is not crucial for the calculation of turbulence quantities. In smaller scales, the noise level of the sensors and the disturbance by the rotor dominate; therefore, a low-pass filter is used in the data processing so that small scales are neglected. Additionally, a combined temperature and humidity sensor is mounted on each UAS. In the current system, the capacity of the battery was increased compared to a previous measurement campaign (Wetz et al. 2021) so that measurement times of 14 min could be reached.

### 2.2 Measurement Campaign

In June/July 2021, we participated in the FESSTVaL campaign (Field Experiment on Sub-Mesoscale Spatio-Temporal Variability in Lindenberg) at the Lindenberg Meteorological Observatory - Richard-Aßmann-Observatory (MOL-RAO) operated by the German Meteorological Service (Deutscher Wetterdienst, DWD). In particular, we operated our fleet at the Boundary Layer Field Site (Grenzschichtmessfeld, GM) in Falkenberg, which includes various atmospheric measurement devices at the site. The most relevant for our purpose is the 99 m mast, which is equipped with multiple sensors at different altitudes. At 90 m and 50 m altitudes, sonic anemometers with a temporal resolution of 20 Hz are mounted. The site is located 80 km south-east of Berlin and can be described as having almost flat, heterogeneous terrain. The land use is dominated by grassland and cropland, including some forest 1 km west of the site. In total, during the 2 weeks (June 21–July 2) of the measurement campaign, more than 1000 single UAS flights were realized.

In Fig. 1, the measurement site is shown, including the 99 m mast, the wind rose of 1 year's (2021) mast measurements at 98 m a.g.l. and different measurement patterns of the UAS-fleet. As the wind rose indicates, the site is dominated by westerly winds, which also applies to the two-week measurement campaign, in which most of the flights can be assigned to westerly

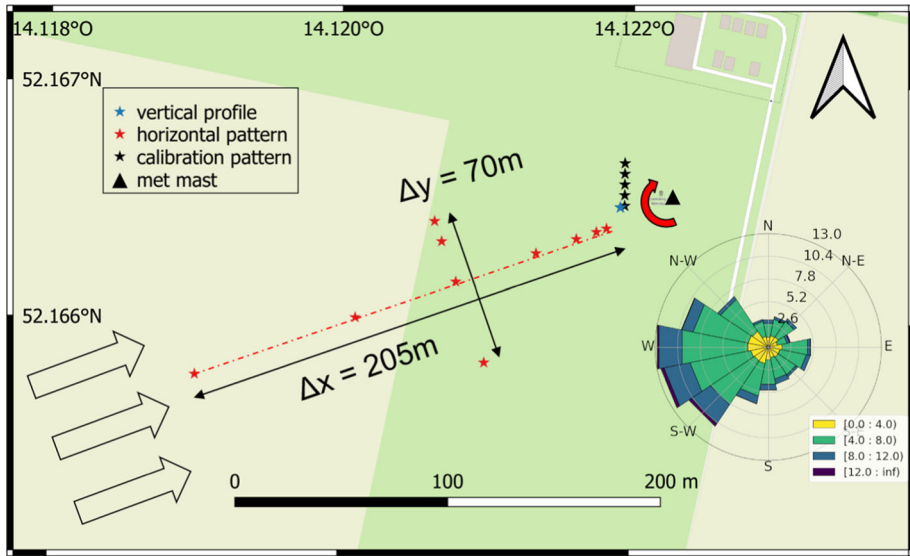


**Fig. 1** Map of the field site of GM Falkenberg, including the 99 m meteorological mast and different flight patterns of the UAS-fleet. Each star represents an individual UAS at its measurement position. The dark green area is short cut grass, whereas the light green area was a cornfield in 2021. The arrows on the left side represent the wind direction and the corresponding orientation of the ‘horizontal pattern’. Background map ©OpenStreetMap contributors 2022. Distributed under a Creative Commons BY-SA License. The wind rose is extracted from the meteorological mast at 98 m a.g.l

winds. Within the map, the stars represent single UAS in their hover position. The flight ‘calibration pattern’ indicates multiple UAS in a line in front of the mast at the corresponding sonic measurement heights of 90 m and 50 m. This pattern was mainly used for calibration and validation purposes, as described in Wetz and Wildmann (2022). Further, vertical profiles were measured continuously with a single UAS or with multiple stacked UAS at different altitudes marked with the flight pattern ‘vertical profile’. Most relevant for this study is the ‘horizontal pattern’ which is used for examining turbulence structures in the ABL. In this pattern, multiple UAS are distributed longitudinally and laterally to the mean wind direction at different distances. The pattern was generated semi-automatically in order to adapt the orientation of the pattern to the current wind direction (illustrated by the red curved arrow in Fig. 1), which was observed from the 99 m mast shortly before each flight. The horizontal spacings between the UAS were chosen to allow for a maximum of different separation distances that can be achieved by combining different UAS. The separation distances in longitudinal direction  $\Delta x$  vary from 5 to 205 m and in lateral direction  $\Delta y$  from 10 to 70 m. The shape of the pattern remained similar throughout the campaign and was arranged at different altitudes and for different thermal stratifications: stable (SABL), neutral (NABL), and convective (CABL). This pattern enables horizontal correlation and coherence studies within the ABL.

**Table 1** Classification of atmospheric stability adapted from Mohan (1998)

Stability class	$Ri_b$
Unstable	$< -0.011$
Near neutral	$-0.011 < Ri_b < 0.042$
Stable	$> 0.042$

### 3 Methodology

#### 3.1 Wind Algorithm

In Wetz and Wildmann (2022) the calculation of the horizontal wind vector that is used in this study is described in detail. The algorithm is based on the principle of aerodynamic drag and relates the horizontal forces to wind speeds. The forces are derived from the equations of motion in the body frame of the multicopter. Acceleration and attitude data from the inertial measurement unit are used as input data for the wind algorithm. The UAS data are calibrated and validated against the sonic measurements from the 99 m mast. The relation between the wind speed and the horizontal forces is modeled with an exponential function. The calibration result of an independent validation dataset yields a RMSE (root-mean-square error) of  $0.25 \text{ m s}^{-1}$  for the mean wind speed and  $0.16 \text{ m}^2 \text{ s}^{-2}$  for the longitudinal, respectively  $0.08 \text{ m}^2 \text{ s}^{-2}$  for the lateral variance. The accuracy of the wind direction measurement is  $4.5^\circ$ . In Wetz and Wildmann (2022) we also found that the temporal resolution of wind measurement is limited to 2 Hz due to sensor noise, which dominates at small scales. This is crucial in low turbulence conditions with a low signal-to-noise ratio.

#### 3.2 Atmospheric Conditions

In order to characterize the atmospheric conditions during the analyzed flights, the dynamic stability is determined with the bulk Richardson number:

$$Ri_b = \frac{|g|\Delta\theta_v\Delta z}{T_v[\Delta u^2 + \Delta v^2]}, \quad (2)$$

which is defined as the ratio of buoyancy energy to shear-kinetic energy (Stull 2016). In Eq. 2 the variables  $\Delta\theta_v$ ,  $\Delta z$ ,  $\Delta u$ ,  $\Delta v$  are the differences over height of virtual potential temperature, altitude, zonal and meridional wind component and  $T_v$  is the virtual temperature. The atmosphere is dynamically unstable if the bulk Richardson number is smaller than the critical Richardson number  $Ri_c = 0.25$ . During the horizontal flight pattern, additional flights for vertical profiling were performed. From these flights the bulk Richardson number could be calculated. However, we use the data of the sonic measurements from 50 and 90 m altitude to calculate the bulk Richardson number, since vertical profiling flights are not available for every analyzed flight. In order to classify the dynamic stability of the ABL, the  $Ri_b$  is used as originally proposed by Mohan (1998) and also applied by Cantero et al. (2022). In this study we refer to the original classification for unstable and stable conditions by Mohan (1998). We define a weakly stratified ('near neutral') class by combining their 'weakly unstable', 'neutral' and 'weakly stable' classes (Table 1).



The height below which the shear production of turbulence exceeds buoyant production is defined by the Obukhov length  $L_O$  (Stull 2016):

$$L_O = \frac{-\overline{\theta_v} u_\star^3}{k |g| (\overline{w'\theta_v'})}, \quad (3)$$

where  $k$  is the von Kármán constant with a value of 0.4 and  $g$  the gravitational acceleration. The turbulent kinematic heat flux  $\overline{w'\theta_v'}$  is defined by the fluctuations of the virtual potential temperature  $\theta_v$  and the vertical velocity  $w$ . The friction velocity is defined by  $u_\star$ . The Obukhov length is calculated at 2 m a.g.l. from sonic anemometer measurements to represent the surface layer characteristics. The surface-layer scaling parameter  $\zeta_O$  (or Monin-Obukhov stability parameter) is often used for static stability characterizations and is defined as:

$$\zeta_O = \frac{z}{L_O}. \quad (4)$$

Statically stable conditions are found for positive  $\zeta_O$  values and unstable conditions for negative  $\zeta_O$  values, wherein the magnitude defines stronger or weaker stability conditions. For example, large, negative values amplify strong, unstable conditions. The Monin-Obukhov stability parameter is listed in Table 2 as a parameter of surface layer stability. The Brunt–Väisälä frequency  $N_{BV}$  sets the upper limit for internal wave frequency in the boundary layer and is defined as:

$$N_{BV}^2 = \frac{g}{\theta_v} \frac{\delta\theta}{\delta z}. \quad (5)$$

It is only defined for stable stratification. Higher  $N_{BV}$  frequencies indicate more stable conditions. In the present study, the Brunt–Väisälä frequency is calculated for the same height as that used for the bulk Richardson number (between 90 m and 50 m). In Table 2, the surface layer parameters based on the Obukhov length in 2 m a.g.l. are listed, as are the Brunt–Väisälä frequency and the bulk Richardson number between 50 and 90 m a.g.l. Due to the different considered altitudes, the derived stability deviates. Particularly, for flight #84 in the early morning hours, the boundary layer between 50 and 90 m according to the  $Ri_b$  is still within the nighttime inversion layer, while the parameters at the surface layer in 2 m a.g.l. already indicate buoyant forces close to the ground. Since the lowest altitude of the considered flights is 50 m a.g.l., we refer to the derived Richardson number  $Ri_b$  between 90 and 50 m for classification of the flight cases.

Another step of quality control is the stationarity test. This test examines whether the atmospheric conditions can be considered stationary during a flight by comparing the velocity variances of sub-divided time intervals  $\overline{\sigma_{u,SI}^2}$  to the variance of the whole time series  $\overline{\sigma_{u,WI}^2}$ . The stationarity is thus quantified by the parameter:

$$St_u = \left| \frac{\overline{\sigma_{u,SI}^2} - \overline{\sigma_{u,WI}^2}}{\overline{\sigma_{u,WI}^2}} \right| \cdot 100\%. \quad (6)$$

For our study, we subdivided the series into four, five and six time intervals and took the mean value of the different intervals. The test has been carried out for the velocity component in lateral and longitudinal directions. The threshold for assuming stationarity is defined as  $St_u < 30\%$  (Foken and Wichura 1996).



### 3.3 Horizontal Correlations

The cross-correlation function  $\rho_{uu_{\Delta x}}(\tau)$  between different UAS measurements of the longitudinal velocity component ( $\Delta x$  meaning the longitudinal separation distance between two UAS) as a function of the time shift  $\tau$  is defined according to:

$$\rho_{uu_{\Delta x}}(\tau) = \frac{\overline{u'(t)u'_{\Delta x}(t + \tau)}}{\sigma_u \sigma_{u_{\Delta x}}}, \quad (7)$$

as the covariance, normalized by the individual standard deviations  $\sigma_u$  (Pope 2000). The velocity fluctuations  $u'$  are derived from the Reynolds decomposition:

$$u' = u - \bar{u}, \quad (8)$$

averaging the velocity  $u$  over the time interval of one single flight of 12 min in order to obtain the mean (advection) velocity  $\bar{u}$ .

The autocorrelation function  $\rho_{uu}(t)$  is defined as the correlation of a variable with itself. For the determination of the integral length scale  $L_x$ , the autocorrelation function of the streamwise wind velocity is first used to derive the Eulerian turbulent time scale  $T_x$  (Lenschow and Stankov 1986). In order to calculate the length scale from the time scale at one measurement point, the frozen turbulence assumption by Taylor is applied (Taylor 1938). The Taylor-Hypothesis states that turbulence remains frozen while passing through the sensor, such that the time scales can be transformed into length scales by multiplication with the advection velocity  $\bar{u}$  (Eq. 10). The advection velocity is calculated by the velocity mean of the time interval of one flight (12 min). Following the approach of Lenschow and Stankov (1986), the time scale is calculated by the integral of the autocorrelation function until the first zero crossing ( $T_0$ , Eq. 9):

$$T_x = \int_0^{T_0} \rho_{uu}(t) dt, \quad (9)$$

$$L_x = T_x \bar{u}. \quad (10)$$

Another way to calculate the integral length scale is to use spatial cross-correlations of the streamwise velocity. This approach is examined in Sect. 4.

### 3.4 Coherence

The coherence between two velocity time series describes the frequency-dependent similarity of the flow structure. The (magnitude-squared) coherence  $\gamma_{uu_{\Delta x}}^2(f)$  of two time series  $u(t)$  and  $u_{\Delta x}(t)$  is defined as the square of the absolute value of the cross-spectrum  $S_{uu_{\Delta x}}(f)$  normalized by the individual power spectra  $S_{uu}(f)$  and  $S_{u_{\Delta x}u_{\Delta x}}(f)$  (see Eq. 15). The cross-spectrum can be calculated by the Fourier transformation of the cross-covariance function  $C_{uu_{\Delta x}}(\tau)$ , which simply is the cross-correlation function (Eq. 7) without normalization:

$$S_{uu_{\Delta x}}(f) = \int_{-\infty}^{\infty} C_{uu_{\Delta x}}(\tau) e^{2\pi i \tau f} d\tau. \quad (11)$$

Equivalent to the cross-spectrum, the power spectrum  $S_{uu}(f)$  can be calculated by the Fourier transformation of the auto-covariance function. Following Lumley and Panofsky (1964), the cross-spectrum can be decomposed into the cospectrum  $Co_{uu_{\Delta x}}(f)$  (real part) and the

quadrature spectrum  $Q_{uu_{\Delta x}}(f)$  (imaginary part):

$$S_{uu_{\Delta x}}(f) = \text{Co}_{uu_{\Delta x}}(f) - iQ_{uu_{\Delta x}}(f) \quad (12)$$

The cospectrum is used, for example, to investigate the spectral distribution of heat flux (Bange et al. 2002). From the cross-spectrum, the phase(-spectrum) can be calculated as the angle between the co- and the quadrature-spectrum:

$$\Phi_{uu_{\Delta x}}(f) = \tan^{-1} \frac{Q_{uu_{\Delta x}}(f)}{\text{Co}_{uu_{\Delta x}}(f)} \quad (13)$$

The amplitude-spectrum  $A_{uu_{\Delta x}}(f)$  refers to the absolute of the complex cross-spectrum:

$$A_{uu_{\Delta x}}(f) = \sqrt{\text{Co}_{uu_{\Delta x}}^2(f) + Q_{uu_{\Delta x}}^2(f)} \quad (14)$$

Note that in literature also the root-coherence and co-coherence are mentioned (Cheynet et al. 2016). In this study, we refer to the magnitude-squared coherence:

$$\gamma_{uu_{\Delta x}}^2(f) = \frac{A_{uu_{\Delta x}}(f)^2}{S_{uu}(f)S_{uu_{\Delta x}}(f)} \quad (15)$$

That means that the phase is not considered here. The coherence only takes values between zero and unity according to Schwartz's inequality. Unity is only reached when the Fourier components of  $u$  and  $u_{\Delta x}$  have proportional amplitudes throughout the ensemble (Lumley and Panofsky 1964).

Since in atmospheric sciences we often rely on only one or a few realizations in a limited time frame, the statistical relevance needs to be evaluated. In the case of coherence estimations, the trade-off is between resolvable scales and statistical errors. This balance depends on the so-called degree of freedom  $M$  which is defined as the product of the subdivided number of segments and the number of averaged spectral estimates. Assuming that we subdivide a time series into 8 small segments and additionally average over four frequencies, we get a degree of freedom of  $M = 8 \cdot 4 = 32$ . In order to calculate the coherence between two time series, each series must be subdivided into at least two shorter segments. Kristensen and Kirkegaard (1986) studied the sampling issues with spectral coherence and proposed an error calculation of the sampled coherence depending on  $M$  and  $\gamma^2$ . This error calculation reveals that an overestimation of the coherence is always found for a finite value of  $M$ . The overestimation and the standard deviation of the coherence estimation reduce with increasing values of  $M$  and  $\gamma^2$ .

Carter et al. (1973) proved an increase of the accuracy of sampled coherence by applying an overlapping of the segments by 50 %. Due to the limited measurement time, we are limited in subdividing the time series into smaller series if the larger scales with high coherence should still be resolved. Therefore, we subdivide the large scales with a degree of freedom of  $M = 4$  with an overlap of 50 % in order to decrease the error. This results in a time frame of 180 s for the present study, leading to maximum resolvable scale of 1 km, assuming an advection velocity of  $6 \text{ m s}^{-1}$ . The smaller scales are calculated with up to  $M = 32$  in order to increase the statistical accuracy. The spectra are computed using Welch's average periodogram method (Bendat and Piersol 2011).

The error calculation according to Kristensen and Kirkegaard (1986) results for the given value of  $M = 4$ , assuming  $\gamma^2 = 0.4$ , in a standard deviation  $\sigma$  of 0.27 (see Eq. 16) and a bias  $B$  of 0.09 (see Eq. 17), for  $\gamma^2 = 0.9$  the standard deviation results in 0.067 and the bias 0.002. Increasing the degree of freedom to  $M = 32$  leads to  $\sigma = 0.09$  and  $B = 0.011$  for  $\gamma^2 = 0.4$ . However, these error estimates are only valid if no window function or overlapping

is included in the coherence calculation, since both functions reduce the error, these estimates need to be understood as an upper limit of the error:

$$B_{\gamma^2} = \gamma^2 + \frac{1}{M}(1 - \gamma^2)^2, \quad (16)$$

$$\sigma_{\gamma^2} = \frac{2}{M}\gamma^2(1 - \gamma^2)^2. \quad (17)$$

### 3.5 Coherence Models

According to the theory of Davenport (1961), the coherence of the streamwise velocity fluctuations between vertically separated measurements can be modeled by an exponential function (see Eq. 1). The coherence decreases both with increasing vertical separation  $\Delta z$  and decreasing wavelength  $\lambda_x = \bar{u}/f$ . The exponential function of the root coherence  $\gamma$  is scaled with a decay constant  $a$  in Eq. 1. Note that Davenport uses the root-coherence  $\gamma$ . In order to compare decay parameters resulting from root-coherence  $\gamma$  and magnitude-squared coherence  $\gamma^2$  the parameter needs to be multiplied by the factor 2 (i.e.  $c_i = 2a$  in Eq. 18). Originally, Davenport formulated the model only for vertical separations, but Pielke and Panofsky (1970) also applied this model to horizontal coherence studies, so that it can be applied for all directions and separation distances  $R$  (if only the longitudinal direction is considered,  $R = \Delta x$ ):

$$\gamma^2(f) = e^{-c \frac{R}{\bar{u}} f}. \quad (18)$$

Schlez and Infield (1998) state that the decay of the coherence depends on the turbulence intensity TI and the horizontal distance between the considered points in space. TI is defined as the ratio of the standard deviation  $\sigma$  to the mean wind velocity  $\bar{u}$  in:

$$TI = \frac{\sigma_u}{\bar{u}} : \quad (19)$$

The longitudinal distance  $\Delta x$  is additionally normalized by the mean velocity  $\bar{u}$ . The rate of decay of the exponential function is defined by the decay parameter  $\alpha_x$  in:

$$\gamma_x^2(f) = e^{-\alpha_x \frac{\sigma_u}{\bar{u}} \frac{\Delta x}{\bar{u}} f}. \quad (20)$$

Schlez and Infield (1998) differentiate between longitudinal and lateral models of the coherence. They state that in the lateral direction the distance  $\Delta y$  between the considered measurements positions should not be normalized by the advection velocity  $\bar{u}$  due to the perpendicular orientation of  $\Delta y$  and advection. Thus, the modeled coherence in the lateral direction is:

$$\gamma_y^2(f) = e^{-\alpha_y \frac{\sigma_u}{\bar{u}} \Delta y f}. \quad (21)$$

As the models of Schlez and Davenport are different, a distinction of the decay parameter is necessary. For clarification we further use the decay parameter  $c$  for the Davenport model and  $\alpha$  for the Schlez model. The decay parameters of the exponential functions are determined from experimental data through a curve fit using the least squares method as described in Moré (1978). In order to compare the scatter of the decay parameters  $c$  and  $\alpha$ , resulting from

different coherence approaches, the relative standard deviation  $d$  is used:

$$d = \frac{\sigma_c}{\bar{c}}, \quad (22)$$

wherein  $\sigma_c$  represents the standard deviation, normalized by the mean of the decay parameter  $\bar{c}$ .

### 3.6 Data Filtering

The 26 available flights of the FESSTVaL campaign with a ‘horizontal pattern’ are filtered for further processing with respect to two criteria: first, the misalignment  $\beta$  of the flight pattern to the mean wind direction is limited to  $30^\circ$ , so that the assumption of longitudinal and lateral separations is coarsely valid. Second, the stationarity test is applied for the streamwise and lateral wind components, and only flights with  $ST < 30\%$  are used for the analysis. From 26 flights during the campaign, only 12 remain, which is mainly due to large misalignment angles that occur in low wind conditions. The flights of the ‘horizontal pattern’ used in further analysis are listed in Table 2.

## 4 Results

### 4.1 Validation of Turbulence Measurements

We have previously shown that the calibration results for the mean wind vector and the velocity variance of the UAS measurements are in good agreement with the reference measurements using the calibration pattern close to the 99-m mast (Wetz and Wildmann 2022). The following analyses are based on the ‘horizontal pattern’ as illustrated in Fig. 1. The capability to measure second order statistics with the UAS is illustrated in Fig. 2a. The amplitude spectra  $A_{uu\Delta x}$  of streamwise velocity fluctuations of two UAS with longitudinal distances of  $\Delta x = 5$  m and  $\Delta x = 205$  m are shown in comparison to the corresponding single-point power spectrum of the sonic anemometer at the mast and a power spectrum of the individual UAS which is closest to the mast. It is evident that, for this neutrally stratified atmosphere, the amplitude spectra and the power-spectrum of the UAS agree well with the reference. Remaining differences can likely be attributed to the fact that the closest UAS is still 30 m away from the sonic. Figure 2b shows the phase-spectra of two UAS combinations with different separation distances ( $\Delta x = 5$  m and  $\Delta x = 205$  m). Assuming that eddies are transported with the mean advection velocity  $\bar{u}$ , the wavelengths are defined as:

$$\lambda = \frac{\bar{u}}{f}. \quad (23)$$

We expect to find the maximum of the phase-spectrum ( $360^\circ$ ) at that wavelength which corresponds to the separation distance  $\lambda(\Phi = 360^\circ) = \Delta x$ . For larger wavelengths, the theoretical phase-spectrum, expressed in degrees, can be calculated as:

$$\Phi_{uu\Delta x} = \frac{\Delta x}{\lambda} 360^\circ. \quad (24)$$

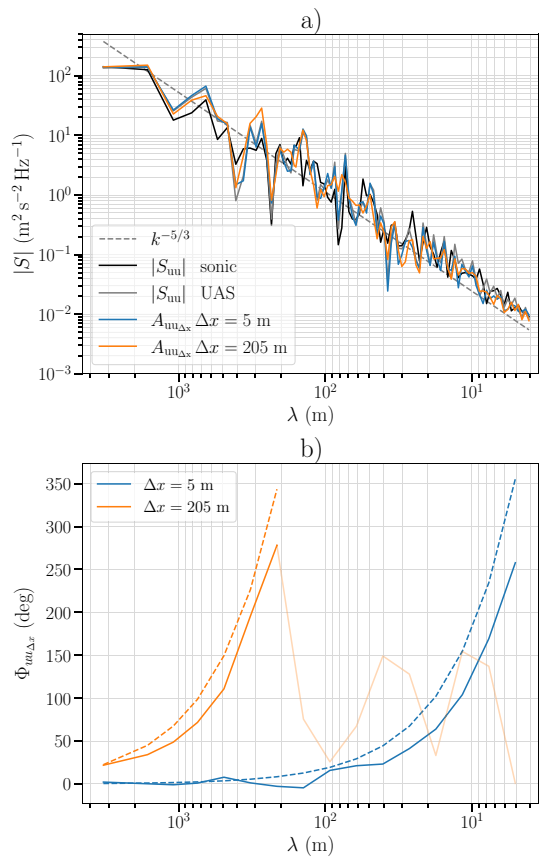
Shorter wavelengths than  $\Delta x$  cannot be adequately represented in the phase-spectrum. The theoretical phase-spectrum is indicated by the dashed lines in Fig. 2b until the separation distances of the considered UAS are reached. The measured phase-spectra in solid lines are

Table 2 Flight protocol of considered flights in Sect. 4 from the ‘horizontal pattern’

Date	Time (UTC)	Flight no.	a.g.l. (m)	$\bar{u}$ (m s <sup>-1</sup> )	$\beta$ (°)	TI (-)	$L_x$ (m)	$L_O$ ( $z = 2$ m) (m)	$\zeta_O$ ( $z = 2$ m) (-)	$N_{BV}$ $\Delta z = 90 - 50$ m s <sup>-1</sup>	$Ri_b$ $\Delta z = 90 - 50$ m (-)	ABL
25.06.2021	12:14	26	50	2.51	24	0.29	108	-4	-0.50	-	-2.427	CABL
25.06.2021	12:40	27	50	1.97	4	0.31	29	-2	-1.00	-	-2.312	CABL
29.06.2021	06:18	87	150	3.71	16	0.162	119	-15	-0.13	-	-0.497	CABL
02.07.2021	12:17	118	90	6.29	1	0.198	329	-40	-0.05	-	-0.137	CABL
02.07.2021	15:12	124	50	6.05	15	0.156	103	-43	-0.05	-	-0.112	CABL
30.06.2021	16:19	101	90	9.26	20	0.209	291	-191	-0.01	-	-0.005	NABL
25.06.2021	15:56	32	50	5.23	27	0.108	143	-29	-0.07	-	-0.001	NABL
30.06.2021	16:52	102	50	8.21	9	0.178	108	-323	-0.01	0.0028	0.006	NABL
30.06.2021	16:05	100	90	8.25	14	0.166	243	-164	-0.01	0.0024	0.01	NABL
30.06.2021	17:05	103	50	7.15	11	0.155	128	-323	-0.01	0.038	0.014	NABL
29.06.2021	03:54	72	90	6.44	17	0.091	87	1	2.00	0.033	0.223	SABL
29.06.2021	05:52	84	150	4.08	20	0.248	153	-20	-0.10	0.01	0.5	SABL

$\beta$  describes the misalignment of the pattern orientation with the mean wind direction. The flights are grouped into convective (CABL), neutral (NABL) and stable (SABL) ABL

**Fig. 2** Power spectrum density  $|S_{uu}|$  of sonic anemometer measurements in comparison to UAS measurements **a** power-spectrum  $|S_{uu}|$  and amplitude spectra  $A_{uu\Delta x}$  and **b** phase-spectra  $\Phi_{uu\Delta x}$  with longitudinal separation of  $\Delta x = 5$  m and  $\Delta x = 205$  m. The thin orange line represents the measured phase for  $\lambda < \Delta x$ . Dashed lines indicate the theoretical phase resulting from the separation distance  $\Delta x$  and the advection velocity  $\bar{u}$  as calculated from Eq. 24 (results from flight no. 100 in Table 2)



shown in light color if they fall below the separation distances, since reasonable results are only expected in the range larger than the spatial spacing of the considered measurements. The results show that the shape of the measured phase-spectra is in line with the theoretical phase. However, a bias can be seen towards shorter wavelengths, which could be explained by the accuracy of the separation distances estimation or by a slightly faster transport velocity of eddies compared to the calculated advection velocity.

In Fig. 3a the integral length scale  $L_x$  in streamwise direction, calculated from UAS measurements, is compared with reference sonic estimates for all flights for which sonic measurements are available in the corresponding flight altitude. The length scale is calculated from the integral over the autocorrelation function as described in Sect. 3, Eq. 10. For the UAS-determined length scale, the median of all ten UAS involved in the flight pattern is calculated. Error bars represent the standard deviation within the fleet. The high  $R$ -value of 0.93 confirms the validity of the UAS estimates. Note that the distances between the UAS and the 99 m mast vary in the longitudinal direction from 30 to 235 m and in the lateral direction up to 40 m. For high length scales in the order of  $L_x > 400$  m the statistical significance of the measurement decreases due to the limited measurement time and thus the number of measured large eddies in one time series. The stable flight cases are associated with low level jets and a strong inversion in the morning hours. The three stable cases presented are from the same morning and show an increase in the turbulent length scale as the day progresses,

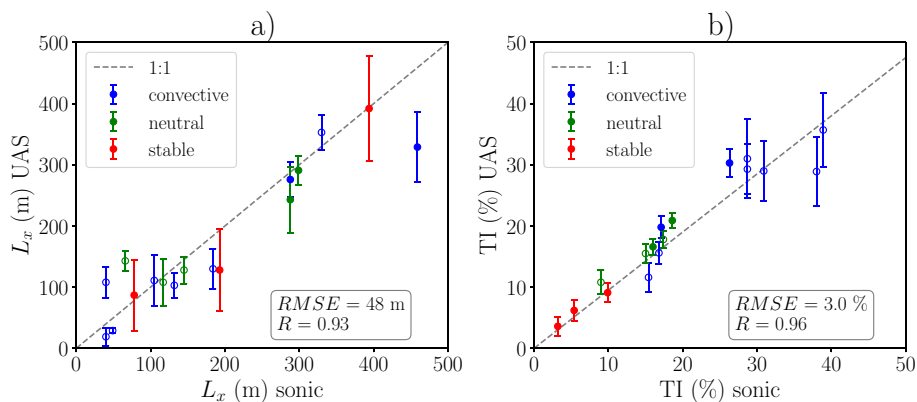


**Fig. 3** **a** Integral length scale  $L_x$  of UAS measurements in comparison to sonic measurements.  $L_x$  for the UAS is calculated by the median of multiple simultaneous measurements. Filled markers are comparisons in 90 m and non filled markers in 50 m a.g.l.. Error bars represent the standard deviation within the fleet. **b** Turbulent intensity  $TI$  of UAS measurements in comparison to sonic measurements. The error bars are calculated by the propagation of uncertainty using the accuracy of the mean velocity and standard deviation of the velocity measurement

resulting in increased development of the convective surface boundary layer. This particular situation, combined with the limited measurement time (12 min) for calculating the length scale, could cause high turbulent length scales even in the SABL.

As mentioned in Sect. 3.5, the decay parameter of the coherence can depend on the turbulence intensity ( $TI$ ). To validate the measurements by the UAS, Fig. 3b shows  $TI$  as measured by the UAS in comparison to the sonic. Since a high accuracy was reached for the mean wind speed and the variance measurements (Wetz and Wildmann 2022),  $TI$  estimates are also quite accurate, with an  $RMSE$  of 3 % and an  $R$ -value of 0.96. The comparatively large error bars for high turbulent intensities are due to low wind speeds and the corresponding larger relative wind speed uncertainties, which are present for cases of  $TI > 0.25$ .

## 4.2 Horizontal Correlation

The objective of the analyses of horizontal correlations is to examine the differences between the actual measurements and the theoretical behavior that would be expected for frozen turbulence. Therefore, in Fig. 4 the cross-correlation  $\rho_{uu_{\Delta x}}$  within the fleet in the horizontal pattern in the longitudinal direction is shown. The UAS closest to the tower is cross-correlated with the remaining six UAS in the longitudinal direction, resulting in horizontal separation distances between 5 m and 205 m. The vertical dashed lines mark the theoretical advection time that the flow needs to travel from the upstream UAS to the reference UAS. It is close to the maxima of the cross-correlations for all distances. However, a slightly faster transportation is observed in the cross-correlation maxima compared to the advection velocity, which is in line with the observations that were made in the phase spectrum of the same flight. A detailed comparison between the travel time of the eddies and the advection time using Taylor's hypothesis is given in Fig. 13 in Appendix by the time lag error of the correlation maxima in relation to the theoretical lag.

The cross-correlations of UAS measurements in Fig. 4 are extended by all possible combinations of UAS in the pattern in order to obtain more grid points for the analysis. The decay of the maxima with increasing separation distance is shown in Fig. 5a. The atmosphere during



**Fig. 4** Cross-correlation function of streamwise velocity between the longitudinally aligned UAS for flight # 100. Dashed vertical lines are the theoretical time lags of the correlation maxima calculated with Taylor's hypothesis. Colored points mark the intersection between the correlation functions and  $\tau = 0$

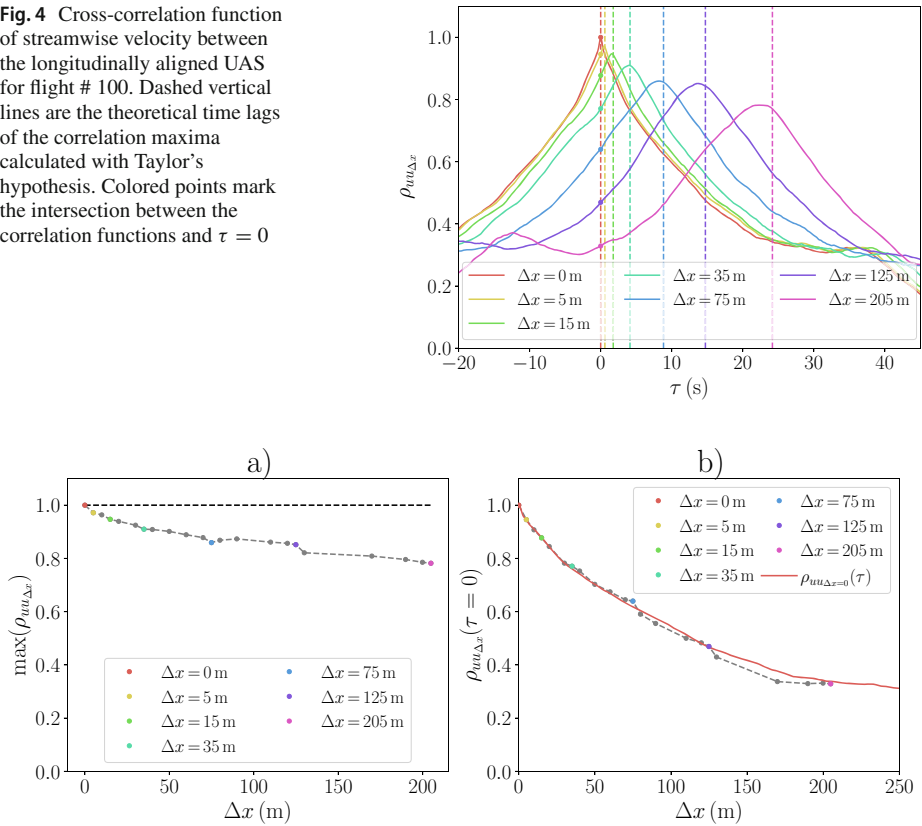


**Fig. 5** **a** Cross-correlation function maxima (from Fig. 4) of all longitudinal combination of UAS with corresponding longitudinal separation distances  $\Delta x$ . **b** Autocorrelation  $\rho_{uu\Delta x=0}(\tau)$  in comparison to direct spatial cross-correlation using the intersection of the cross-correlation function  $\rho_{uu\Delta x}$  and  $\tau = 0$ , marked as dots in Fig. 4 for flight # 100

the studied flight (# 100 in Table 2) was neutrally stratified with a bulk Richardson number of  $Ri_b = 0.01$ . The mean wind speed was  $\bar{u} = 8.3 \text{ m s}^{-1}$  with a TI of 0.17 and an integral length scale of  $L_x = 245 \text{ m}$ . The fact that the maxima decrease with distance is strictly speaking in disagreement with Taylor's hypothesis, which implies that the maxima of the cross-correlation function should be unity if turbulence is frozen and only advected.

Subsequently, the maxima of the cross-correlation function for different atmospheric conditions are evaluated in Fig. 6. We observe that the maxima decay more strongly in stable and convective conditions compared to neutral conditions. While not explicitly shown here, we also observed stronger decays in lower heights. This means that the frozen turbulence assumption is more valid in neutral stratified boundary layers and in greater distance to the ground.

The autocorrelation of a single point measurement of the wind velocity is frequently used to study horizontal scales of turbulence under the assumption of frozen turbulence. With our data we can compare the single point autocorrelation  $\rho_{uu}$  with spatial cross-correlation. For this purpose the intersection of the cross-correlation function with the y-axis ( $\rho_{uu\Delta x}(\tau = 0)$ ) in Fig. 4, which is equal to the correlation coefficient of two spatially separated measurement points, is determined. Similar to the maxima in Fig. 5a, the correlation coefficients can

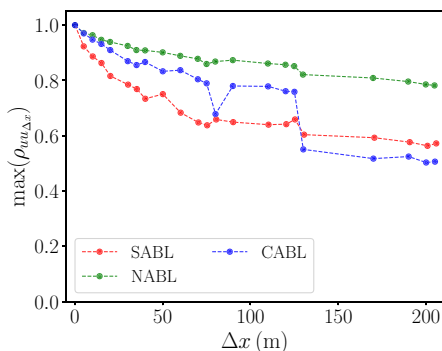


**Fig. 6** Cross-correlation function maxima (identical derived as Fig. 5a) for CABL (# 118), SABL (# 72) and NABL (# 100) in 90 m a.g.l

be plotted for a multitude of UAS combinations (i.e., different separation distances). This collection of correlation coefficients is compared with the autocorrelation function of the reference UAS in Fig. 5b. The time shift  $\tau$  of the autocorrelation function is converted to a theoretical spatial shift  $\Delta x$  by the advection velocity  $\bar{u}$ . In this particular flight, the direct spatial cross-correlation is well approximated by the autocorrelation, thus the assumption of Taylor can be considered to be applicable. Further, the spatial correlation can additionally be used for a direct calculation of the ILS without the need for the frozen turbulence assumption.

In Fig. 7, the spatial cross-correlations are compared to the reference UAS autocorrelation, as in Fig. 5b, but for different atmospheric conditions (Fig. 7a) and measurement heights (Fig. 7b). In the neutrally stratified boundary layer, the autocorrelation is closest to the cross-correlation, thus the estimation of ILS from a single time series can be expected to be in good agreement with an estimation from spatial correlation. The deviation between the curves of the different approaches increases for stable and convective conditions as well as in lower altitudes.

The significant drop of the cross-correlations in convective conditions that can be seen in Fig. 7 and also in Fig. 6 at  $\Delta x = 80$  m and  $\Delta x > 125$  m is connected to combinations with the UAS in the far west. The decay of the autocorrelation function of this UAS is much steeper than for all other UAS in the pattern, thus the involvement of this UAS leads to smaller cross-correlations. To preclude any technical issues with the particular UAS itself, we checked a calibration flight that was performed in between both convective cases (flight 118 and # 124). The autocorrelations during this calibration flight, where individual UAS are only separated by 5 m each, are in very good agreement throughout the fleet. Therefore, the difference in the correlation of this UAS in the horizontal pattern could well be due to atmospheric features. An explanation could be the different surface land-use at the location of this UAS. As can be seen in Fig. 1 the far west UAS measures over corn fields while the other involved UAS are hovering over grasslands. Particularly in convective conditions, it is conceivable that such a difference in land-use can cause considerable differences in turbulent structures. This result suggests that spatial measurements can reveal atmospheric features that can not easily be observed from single point measurements.

### 4.3 Horizontal Coherence

The cross-correlation function describes how the time series of horizontally separated UAS measurements are related. The coherence additionally provides information about the simi-

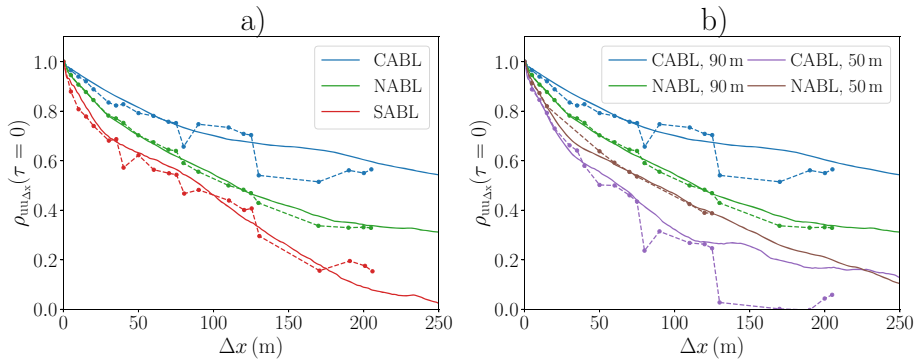


**Fig. 7** Cross-correlation within the UAS-fleet of  $\tau = 0$ , dots and dashed line, in comparison to autocorrelation of single UAS, solid line, for **a** different atmospheric conditions in 90 m a.g.l. and **b** different altitudes (50 m a.g.l. and 90 m a.g.l.). Flight numbers in **a**): 72 (SABL), 100 (NABL), 118 (CABL) and **b**): 100 (90 m, NABL), 102 (50 m, NABL), 118 (90 m, CABL), 124 (50 m, CABL)

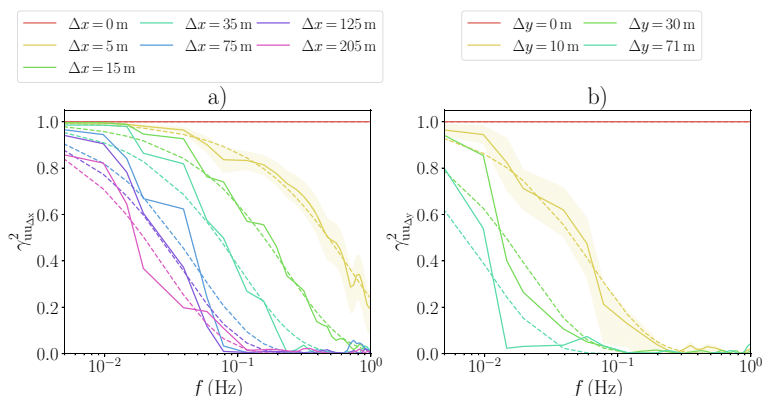
larity of flow structures in the frequency space. The intention of this section is to show the capability of the UAS-fleet to determine coherence in the ABL. In the following section, the measurement results are then compared to coherence models to show their applicability and limitations.

Figure 8 shows the longitudinal (a) and lateral (b) coherence of the streamwise velocity fluctuations depending on the frequency for different separation distances  $\Delta x$  and  $\Delta y$  in a neutral ABL. The longitudinal coherence  $\gamma_{uu_{\Delta x}}^2$  is calculated between the closest UAS to the mast and other UAS in longitudinal direction with different separation distances  $\Delta x$  to the reference UAS (see Eq. 15). As expected, the coherence decreases with increasing distance and frequency. The dashed lines outline the corresponding model with an exponential function (see Eq. 18) using individual decay parameters. Additionally, the uncertainties described in Sect. 3 for the chosen degree of freedom  $M$  are indicated by the yellow shading for the smallest separation distance of each direction. In lateral direction, only four UAS were aligned. The decay of the lateral coherence is stronger at large scales compared to the longitudinal coherence, but can also be modeled with exponential functions (see Fig. 8). The stronger decay of coherence leads to a smaller frequency range in which flow similarity can be assumed.

#### 4.4 Analysis of Coherence Models

Before we compare the measurement results with coherence models, we need to reduce the dataset for a valid comparison and clarify restrictions, both for the measurements and coherence models.

The coherence at low frequencies does not reach unity if  $\Delta x$  exceeds the integral length scale  $L_x$  and the applicability of an exponential decay model is limited in such a case. This is observed at low altitudes and under stable atmospheric conditions, where  $L_x$  is typically small. Furthermore, the time of a single hover flight of approximately 12 min is not sufficient for studying the coherence of large separation distances, since the necessary sub-division of the time series only allows an analyzes up to a frequency at which the coherence has not yet reached its maximum. Due to those restrictions, we only estimate decay parameters for  $\Delta x$  which are small enough to provide solid estimates and compare them for different conditions.



**Fig. 8** Coherence of streamwise velocity fluctuations of **a** longitudinally separated UAS measurements and **b** laterally separated measurements on the right side for flight no. 100. In dashed lines, corresponding approximations with exponential decay function (Eq. 18) using individual decay parameters are shown. Uncertainties of the coherence estimation (Sect. 3) are indicated by the yellow shadow for one separation distance of each direction

Longitudinal distances  $> 35$  m and lateral distances  $> 10$  m lead to coherence values which are smaller than unity in the large scales for the current measurement setup. As mentioned in Sect. 3.5, the bias and the uncertainty of the coherence calculation rise with decreasing coherence. Only separation distances smaller than  $\Delta x \leq 35$  m and  $\Delta y \leq 10$  m are thus considered.

In the following, we compare two of the analytical models for coherence as presented in Sect. 3.5. First, we apply the Davenport (1961) decay model, which is equal in both directions. The coherence model of Schlez and Infield (1998) is then examined, including different models for lateral and longitudinal coherence. The comparison of the models is performed by evaluating the dependency of the decay parameter on the turbulence intensity, since that is the most critical distinction between the two models.

#### 4.4.1 Model Comparison Based on Their Dependency on Turbulence Intensity

The decay parameters for all flights, independent of altitude and atmospheric conditions, are shown in Fig. 9 over turbulent intensity TI for longitudinal (a) and lateral (b) direction. Here, the decay parameters are compared between the Davenport model (blue) and the extended model of Schlez (orange). We observe no clear dependency of the decay parameter  $c_x$  and  $c_y$  on the turbulent intensity. Despite the fact that Schlez and Infield (1998) (Eq. 20) included the turbulence intensity in their model, the results are not improved compared to Davenport. A universal decay parameter can hardly be used to describe a coherence model for the whole dataset. A wide scatter remains, which is likely due to the wide range of atmospheric conditions in the dataset.

#### 4.4.2 Dependency of Davenports Coherence Model on Atmospheric Conditions

In addition to the question of the dependency on the turbulence intensity, it is examined whether the coherence decay parameter depends on the atmospheric stability. In Fig. 10, the different decay parameters are classified according to the dynamic stability (i.e. bulk

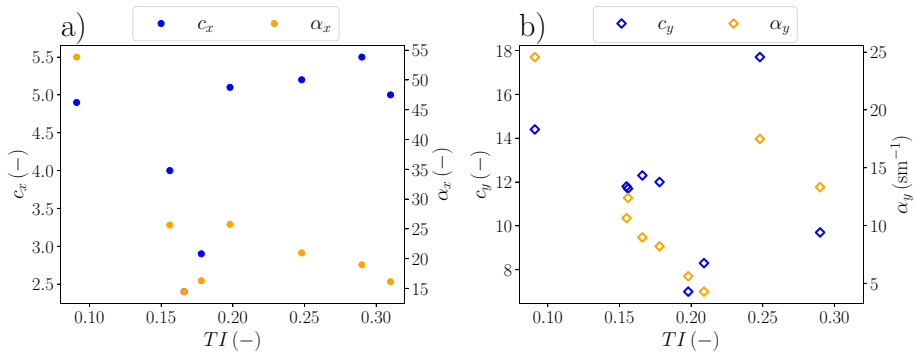


**Fig. 9** Coherence decay parameter for Davenport  $c_x$ ,  $c_y$  and for Schlez  $\alpha_x$ ,  $\alpha_y$  approach for **a** longitudinal and **b** lateral direction in dependency of turbulent intensity TI, with separation distances of  $\Delta x = 5$  m and  $\Delta y = 10$  m

**Fig. 10** Coherence decay parameter for the Davenport approach  $c_x$ ,  $c_y$  for longitudinal  $x$  and lateral direction  $y$  in dependency of the dynamic stability classes defined in Table 1 based on  $Ri_b$ , with separation distances of  $\Delta x = 5$  m and  $\Delta y = 10$  m

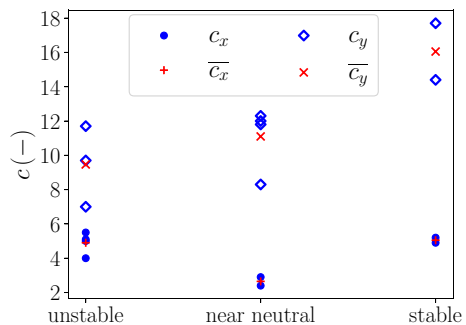


**Table 3** Measured mean decay parameters after Davenport model in longitudinal  $c_x$  and lateral direction  $c_y$  for the 12 considered flights classified by the atmospheric conditions

	CABL	NABL	SABL
$\overline{c_x}$	4.9	2.4	4.8
$\overline{c_y}$	9.5	11.1	16.1

Richardson number  $Ri_b$ ). In this figure, only the Davenport decay parameters are shown, since the results of the Schlez model do not show clear improvements. Regarding the different directions, it is evident that the decay parameters in the lateral direction  $c_y$  take higher values, which indicates less coherence of the flow structure compared to the longitudinal direction ( $c_x$ ). Considering the lateral direction, the scatter within the different atmospheric conditions is wide. However, regarding the average values, a decrease in coherence could be observed with increasing stability. For clarification, a stronger decrease in coherence leads to a larger decay parameter. In longitudinal direction, the coherence is highest for neutral conditions and decreases in stable and unstable conditions (Table 3). Figure 10 only shows the values for  $\Delta x = 5$  m and  $\Delta y = 10$  m, which are the smallest separation distances.

**Fig. 11** Approximation of the longitudinal coherence of streamwise velocity fluctuations for different atmospheric conditions and separation distances. The coherence is plotted over the wave number  $k$  and the separation distance  $\Delta x$ . Dashed lines represent different separation distances  $\Delta x$  of 10, 15, 20, 30, 35 m, the color density decreases with increasing distance

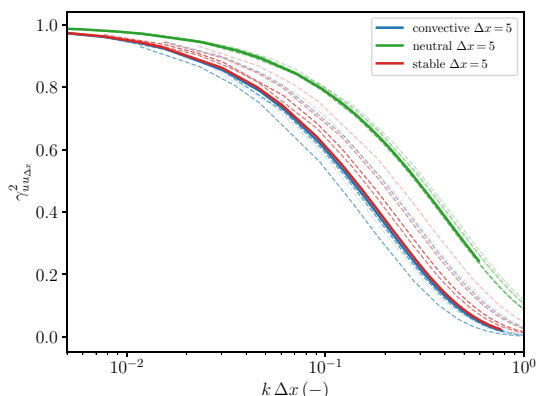
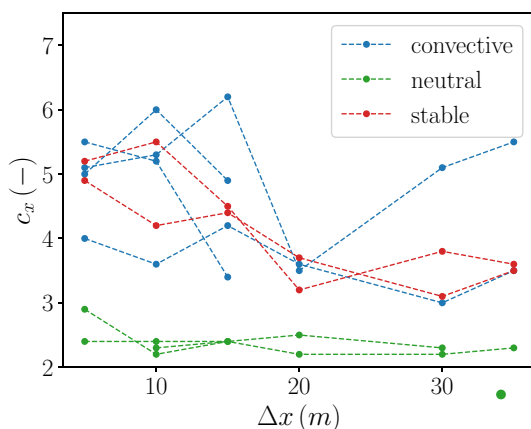


**Fig. 12** Decay parameter  $c_x$  for different atmospheric conditions in dependency of the longitudinal separation distances  $\Delta x$ . Data from simultaneous flights are connected with dashed lines



#### 4.4.3 Dependency of Davenports Coherence Model on Separation Distances

As mentioned before, coherence is a function of the separation distance. In the following, we examine whether the dependency on the separation distances proposed by Davenport is generally applicable under different atmospheric conditions. In Fig. 11, longitudinal coherence curves for three cases with different atmospheric stability classes are presented, i.e. stable, neutral and convective. The coherence is plotted against the product of wave number  $k = \frac{f}{\bar{u}}$  and separation distance  $\Delta x$ . Following the original Davenport model (Eq. 18), the decay of the coherence should only be a function of  $f/\bar{u} \cdot \Delta x$ , thus in Fig. 11 the coherence of different separation distances should be equal. However, this only seems to be adequate in neutral conditions. For stable conditions, the decay decreases with increasing separation distances. In convective conditions, the decay parameter is more variable than in the neutral case, but less variable than in the stable case.

In order to examine the capability of the Davenport model to reproduce the dependency of the coherence on the separation distances for different atmospheric conditions for multiple flights, the decay parameter  $c_x$  is shown in dependency of the longitudinal separation distance for different atmospheric stability regimes in Fig. 12. During two of the convective cases, the wind velocity was less than  $3 \text{ m s}^{-1}$  and the integral length scale was too small, so that a determination of  $c_x$  for separation distances larger than 15 m was not reasonable. Only very small coherence is observed in the low frequencies in such cases. Due to that, two curves of convective conditions in Fig. 12 end at  $\Delta x = 15 \text{ m}$ . For some flights in neutral conditions, the

pattern was incomplete due to technical issues with individual UAS, so that some separation distances are missing. Overall, it can be observed that in neutral conditions  $c_x$  is almost constant over distance. For the stable cases, a decrease of the decay parameter with distance is clearly visible. In convective conditions, the scatter is wider and a trend can not be clearly seen.

## 5 Discussion

### 5.1 Comparison of the Davenport and Schlez Model

Modeling coherence with an exponential function using the Davenport approach and the further extension by Schlez et al. were originally proposed for neutral atmospheric conditions. The dependency between coherence and separation distance for neutral conditions described in the model is confirmed by Fig. 11. However, in convective and stable conditions, the models are not universally valid. In stable conditions, the decay parameter significantly decreases with increasing distance, although the separation distance is included as a parameter in the model. This dependency of the decay parameter on separation distance in stable conditions is also described by Ropelewski et al. (1973).

In comparison to Davenport, Schlez and Infield (1998) included turbulence intensity into their model, which is a reasonable approach under the assumption that increased statistical turbulence in the flow reduces the coherence. In order to evaluate and compare the scatter of the decay parameters for the Davenport model and the approach by Schlez and Infield (1998), the relative standard deviation  $d$  is used. Considering all filtered data, independent of the atmospheric conditions, the deviation for lateral separations ( $\Delta y = 10$  m) for Davenport is  $d_{D,y} = 0.27$  and for Schlez it is higher with  $d_{S,y} = 0.50$ . In longitudinal direction, for separation distances of  $\Delta x = 5$  m the variation results in  $d_{D,x} = 0.26$  and  $d_{S,x} = 0.51$  for Davenport and Schlez respectively. The results do not show a reduction of the scatter using the Schlez model. In fact, the Davenport model even shows smaller variation in both directions. The relative standard deviation obviously gets smaller if only flights in a neutrally stratified atmosphere are considered. In these conditions, only small differences between the models are found. It thus seems evident that a simple enhancement of the model with turbulence intensity is not adequate for non-neutral stratification.

### 5.2 Comparison to Other Studies

To relate the calculated decay parameter  $c_x$  and  $c_y$  for streamwise velocity component to other studies, we first want to clarify that we are now only referring to the Davenport formulation, and the magnitude-squared coherence  $\gamma^2$ . Shiotani and Iwatani (1980) studied the lateral separation at 40 m height proposing a decay parameter which is a function of the ratio of the separation distance  $\Delta y$  to the height  $z$  resulting in  $a_y = 14(\Delta y/z)^{0.45}$ . Adjusted for the present measurement setup, Shiotani and Iwatani (1980) state a range of  $c_y = 10.4 \dots 13.6$  without distinction of atmospheric stability. The experiment took place at a coast line with high wind speeds of  $15 \dots 40$  m s<sup>-1</sup>. Schlez and Infield (1998) listed various results from the literature for longitudinal and lateral coherence. The decay parameter in longitudinal direction varies mainly in the range of  $c_x = 3 \dots 8$  and in lateral direction  $c_y = 19 \dots 40$ . The experiments that are cited for the lateral direction are not directly comparable due to measurement heights lower than 5 m, separation distances in the range of the integral length



scale, or different surface types such as complex terrain or ice. More relevant for a comparison of lateral coherence is the experiment at the Sotra bridge by Jensen and Kristensen (1979) resulting in  $c_y = 14$  for neutral stratification. In comparison, the results of the current study show a range of the decay parameter for lateral separations of  $c_y = 9 \dots 16$  and for longitudinal separations of  $c_x = 2 \dots 5$ .

### 5.3 Coherence of Lateral Separations

In Fig. 10 an increase of the decay parameter with increasing stability is observed for lateral separations of  $\Delta y = 10$  m which is in accordance with the study by Ropelewski et al. (1973). For lateral coherence, they found a dependency on the ratio of longitudinal to lateral integral length scales, which itself depends on the atmospheric stratification. The ratio of lateral to longitudinal coherence also increases for stable conditions in comparison to convective ABL. This can be explained by the more narrow shape of turbulent eddies in stable conditions in comparison to a more circular shape in convective conditions. Overall, the results in literature range from  $c_x = 3 \dots 10$  and from  $c_y = 9 \dots 30$ , examining various experiments and atmospheric conditions.

For studying the coherence of large separations in the range of the integral length scale, longer measurement times are needed in order to resolve the coherence in larger scales with sufficient accuracy. In particular for stable conditions and for the lateral direction, the coherence is often already very low at comparatively large scales. Theoretically, models can be used that allow for coherence without converging to unity at large scales. However, an additional challenge is that the uncertainty and bias of the coherence calculation are large for small coherence values.

### 5.4 Implications of Coherence on Taylor's Hypothesis

Mizuno and Panofsky (1975) investigated the limits of Taylor's frozen hypothesis. For that purpose, they proposed a model to estimate the maximum distance at which the hypothesis is still valid. Based on the coherence, which should be close to unity if flow similarity is given, the maximum of the valid spatial separation  $\Delta D$  is defined as:

$$\Delta D < L_x \frac{2\pi}{c_x}. \quad (25)$$

It depends on the longitudinal integral length scale  $L_x$  and the coherence decay parameter  $c_x$ . In stable conditions,  $L_x$  is typically small due to the damping of vertical motions in the atmosphere, but the coherence decay parameter is typically higher than in convective cases. Both effects decrease the valid distance of Taylor's hypothesis. If we consider a flight in stable conditions during the morning transition of June, 29 (flight number 72) with  $L_x = 87$  m and  $c_x = 4.5$ , the maximum distance for valid Taylor hypothesis results in  $\Delta D < 121$  m. Compared to a flight in convective conditions (flight number 118),  $L_x = 329$  m and  $c_x = 5.5$  lead to a maximum distance of  $\Delta D < 376$  m. This information can have implications for the experimental setup and how data from stationary point measurements or aircraft flight legs need to be interpreted.

## 5.5 ABL Structures Under Different Atmospheric Conditions

In the atmospheric boundary layer, different shapes and characteristics of turbulence are expected for different stratification. The analysis of the longitudinal spatial cross-correlation (see Fig. 6 and Fig. 7) reveals that under neutral conditions frozen turbulence can be assumed, where the spatial development of turbulence is almost negligible in the considered temporal frame. Additionally, the streamwise coherence of longitudinally separated measurements demonstrates high correlations across a wide frequency range in NABL, indicated by small decay parameters (see Fig. 12). If buoyancy terms are significant, either positive (CABL) or negative (SABL), both the coherence and the cross-correlation decrease for increasing longitudinal separation distance. In the NABL coherence scales more uniformly over the separation distance than in SABL and CABL which indicates less spatial variability of the turbulence structures along the considered measurement positions (see Fig. 12). The cross-correlation and coherence of laterally separated measurements, on the other hand, differ significantly between stable and convective stratification. The horizontal shape of flow structures in convective conditions is more circular due to the higher turbulence mixing, which uniformizes the turbulence structures. In contrast, in stable conditions and also in neutral conditions, as reported by Hutchins and Marusic (2007), the structures are stretched in the longitudinal direction such that the cross-correlation decays faster in the lateral than in the longitudinal direction (see Fig. 14 in Appendix). In general, the coherence of laterally separated measurements is lower than for longitudinal separations independent of the stratification. However, the ratio between the lateral and longitudinal coherence is largest for neutral and stable conditions (see Fig. 10), which supports the more isotropic shape of the turbulence throughout the observed scales in convective conditions.

For more detailed studies of the shape of turbulent structures, laterally and in particular vertically distributed measurements would be favorable in the future. Vertically distributed measurements would enable an analysis of the vertical shapes of the structures using the presented cross-correlation and coherence methods. These results could be compared with studies from Salesky and Anderson (2018, 2019); Chauhan et al. (2012) who examined the vertical structure of turbulence and the structural steepening under different stratification.

## 6 Conclusions

During the FESSTVaL campaign, the SWUF-3D fleet of quadrotors was successfully deployed, showing its great potential for studying correlation and coherence with spatially distributed measurements. The turbulent wind measurements were validated to be in good agreement with stationary reference measurements of sonic anemometers at a meteorological mast. We showed with the analyses of cross-spectra, including amplitude and phase, that frequency-resolved processing of data within the fleet is feasible. For the first time, we showed that multicopter UAS can be used for these kinds of measurements. From the presented dataset and results, we can draw multiple conclusions:

1. With a flight pattern of multiple UAS along a horizontal line, the calculation of streamwise ILS using spatial correlation is enabled. The results are in good agreement with the calculation of ILS using the autocorrelation function of the time series of a single UAS when Taylor's hypothesis is valid in neutral atmospheric stratification. In stable and convective conditions, the comparison shows that Taylor's hypothesis is not unconditionally valid in the considered spatial domain.

2. Coherence of the ABL flow is of particular interest for applications where critical wind loads can lead to fatigue and material failure. Measuring coherence is particularly challenging in the field and we showed that a UAS fleet can be a flexible tool to enable such measurements and deepen the understanding. We focused in this study on a demonstration of the feasibility of such measurements and the analysis of the applicability of basic coherence models in different atmospheric conditions at the flat, but heterogeneous field site Falkenberg. Throughout the dataset, the lateral and longitudinal coherence measured with the UAS fleet, show the expected behavior of decreasing coherence with increasing separation distance and smaller frequency scales. The Davenport coherence model shows less scatter than the Schlez-model for all atmospheric conditions. The dependency on turbulence intensity, as proposed by Schlez, could not be confirmed for the decay of coherence with the analyzed flights.
3. We analyzed the decay parameters of the coherence models with respect to the dynamic stability of the ABL. We found that while the Davenport model can be used well to describe coherence for different separation distances with a constant decay parameter in neutral conditions, a high variability arises in stable and convective conditions.
4. The magnitudes of the decay parameters  $c_x$  and  $c_y$  are in good agreement with other, comparable experiments that are described in literature. For lateral coherence, we found an increase of  $c_y$  with increasing stability, which has also been described in the literature before.
5. With  $L_x$  and  $c_x$ , which can both be determined from the UAS fleet measurements, we also determined the maximum distance of validity for Taylor's hypothesis, which can be of great benefit for future planning of ABL experiments.
6. We could observe that the correlations of one particular UAS, which was furthest away from the other UAS and hovering over a different surface type (cornfield vs. grass), showed significantly different characteristics in convective conditions. This indicates different turbulence structures within a relatively small area and should be investigated in more detail in future.

In future, the results of the coherence can be compared with theoretical models from Mann and von Kármán and with different model approaches that account for coherence only reaching values smaller than one, which are out of scope of this study. With an increased flight time, it will be possible to increase the accuracy of large-scale coherence estimation, which then allows for the analysis of larger separation distances with more robustness. Furthermore, the vertical coherence can also be studied with the UAS-fleet if flight patterns with vertical instead of horizontal alignment of individual UAS are designed. In this context the structural steeping of turbulent structures could be examined by calculating the inclination angle (Chauhan et al. 2012) using vertically distributed measurements. In this study, we only considered the streamwise velocity component, but the component perpendicular to the mean flow is also available and can be analyzed in future. Most recently, we developed new methods to retrieve the vertical wind component as well (Wildmann and Wetz 2022). Using all three wind components, the calculation of the complete coherence tensor becomes possible. Similarly, the calculation of vertical and lateral length scales can be included to gain information about the spatial extent of atmospheric flow structures. Since the fleet of UAS can be deployed most flexibly, we intend to use it in future in more complex terrain, where mast installations are too expensive or impossible. We also see a great potential in the analysis of very instationary turbulent structures such as wind turbine wakes.

**Acknowledgements** We thank the Hans Ertel Centre for Weather Research (HERZ) of DWD for the invitation and organisation of the FESSTVaL campaign and especially Frank Beyrich for his support and the provision

of measurement data from the field site of GM Falkenberg. We thank May Bohmann for her assistance with the UAS measurement campaign. Patrick Vrancken internally reviewed the manuscript and we thank him for his valuable comments. We also thank two anonymous reviewers who helped to improve the manuscript.

**Author Contributions** TW wrote the main manuscript text and prepared figures 2–11. JZ was largely involved in the planning of the experiment and performed basic data evaluations. JB contributed with his expertise to Section 3 in particular. NW was involved in the development process of the UAS and the experiment and prepared Figure 1. All authors reviewed the manuscript.

**Funding** Open Access funding enabled and organized by Projekt DEAL. Funded by the European Union (ERC, ESTABLIS-UAS, 101040823). Views and opinions expressed are however those of the author(s) only and do not necessarily reflect those of the European Union or the European Research Council. Neither the European Union nor the granting authority can be held responsible for them.

**Data availability** The UAS-data are available at Wildmann (2022).

## Declarations

**Competing interest** I declare that the authors have no competing interests as defined by Springer, or other interests that might be perceived to influence the results and/or discussion reported in this paper.

**Open Access** This article is licensed under a Creative Commons Attribution 4.0 International License, which permits use, sharing, adaptation, distribution and reproduction in any medium or format, as long as you give appropriate credit to the original author(s) and the source, provide a link to the Creative Commons licence, and indicate if changes were made. The images or other third party material in this article are included in the article's Creative Commons licence, unless indicated otherwise in a credit line to the material. If material is not included in the article's Creative Commons licence and your intended use is not permitted by statutory regulation or exceeds the permitted use, you will need to obtain permission directly from the copyright holder. To view a copy of this licence, visit <http://creativecommons.org/licenses/by/4.0/>.

## Appendix 1: Cross-Correlation Time Lag Error

The lag error, defined as the theoretical lag using Taylor's hypothesis subtracted by the lag of the cross-correlation maxima, is calculated for all flights. This time lag error is shown in Fig. 13a against the cross-correlation maxima for three different atmospheric conditions. Negative lag errors indicate a faster transport of the eddies than the Taylor advection velocity while positive lag errors are related to a slower eddy transport than the advection velocity. For a better relative comparison, the lag error in Fig. 13b is normalized by the theoretical lag. The results show a wide scatter with a tendency towards negative values, which indicates a faster transport of turbulence structures compared to the mean wind speed. However, for this particular case study, the SABL shows a slower eddy transport than the advection velocity. The physical reason for this behavior in this particular flight would require a more detailed analysis which is out of the scope of this paper.

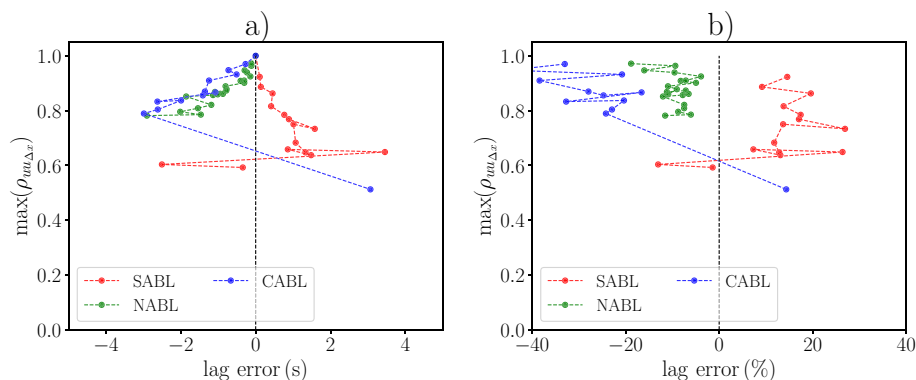
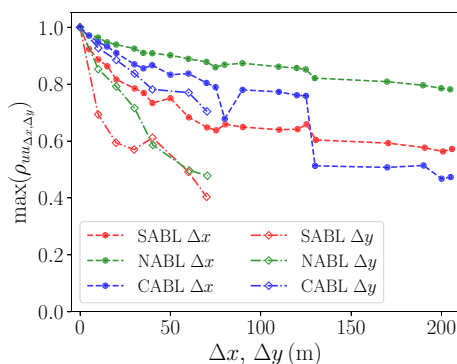


**Fig. 13** Lag error of the cross-correlation maxima lag related to theoretic lag by Taylor in dependency of cross-correlation maxima in seconds **a)** and normalized with the theoretical lag in percent **b)** in 90 m a.g.l. for CABL (# 118), SABL (# 72) and NABL (# 100) in b)

## Appendix 2: Maxima of Cross-Correlation Function, Lateral vs. Longitudinal Separations

In Fig. 14 the maxima of cross-correlation functions are shown against the separation distances in the longitudinal  $\Delta x$  and the lateral  $\Delta y$  direction. This figure outlines the difference in cross-correlation behavior of longitudinal separations, in comparison to lateral separations under different atmospheric conditions. In convective conditions, the ratio between longitudinal and lateral cross-correlations is small, thus the dependency on spatial correlation is weak, which leads to nearly circular shapes of the turbulence structures. However, under stable and neutral conditions the ratios between longitudinal and lateral correlations are much larger which leads to more narrow, in longitudinal direction stretched, turbulence structures.

**Fig. 14** Cross-correlation maxima for longitudinal and lateral distributed measurement against the separation distances  $\Delta x$  and  $\Delta y$  in 90 m a.g.l. for CABL (# 118), SABL (# 72) and NABL (# 100)



## References

- Bange J, Beyrich F, Engelbart DAM (2002) Airborne measurements of turbulent fluxes during LITFASS-98: comparison with ground measurements and remote sensing in a case study. *Theor Appl Climatol* 73(1–2):35–51
- Bendat J, Piersol A (2011) Random data: analysis and measurement procedures. Wiley Series in Probability and Statistics, Wiley
- Cantero E, Sanz J, Borbón F, Paredes D, García A (2022) On the measurement of stability parameter over complex mountainous terrain. *Wind Energy Sci* 7(1):221–235
- Carter G, Knapp C, Nuttall A (1973) Estimation of the magnitude-squared coherence function via overlapped fast fourier transform processing. *IEEE Trans Audio Electroacoust* 21(4):337–344
- Chauhan K, Hutchins N, Monty J, Marusic I (2012) Structure inclination angles in the convective atmospheric surface layer. *Boundary-Layer Meteorol* 147(1):41–50
- Cheyne E, Jakobsen JB, Snæbjörnsson J, Mikkelsen T, Sjöholm M, Mann J, Hansen P, Angelou N, Svandal B (2016) Application of short-range dual-doppler lidars to evaluate the coherence of turbulence. *Exp Fluids* 57(12):184
- Cheyne E, Flüge M, Reuder J, Jakobsen JB, Heggelund Y, Svandal B, Saavedra Garfias P, Obhrai C, Daniotti N, Berge J, Düscha C, Wildmann N, Onarheim IH, Godvik M (2021) The cotur project: remote sensing of offshore turbulence for wind energy application. *Atmos Measure Tech* 14(9):6137–6157
- Cuxart J, Wrenger B, Matjacic B, Mahrt L (2019) Spatial variability of the lower atmospheric boundary layer over hilly terrain as observed with an rras. *Atmosphere* 10(11):715
- Davenport AG (1961) The spectrum of horizontal gustiness near the ground in high winds. *Q J R Meteorol Soc* 87:194–211
- Foken T, Wichura B (1996) Tools for quality assessment of surface-based flux measurements. *Agric For Meteorol* 78(1):83–105
- Heisel M, Sullivan PP, Katul GG, Chamecki M (2022) Turbulence organization and mean profile shapes in the stably stratified boundary layer: zones of uniform momentum and air temperature. *Boundary-Layer Meteorol*
- Higgins CW, Froidevaux M, Simeonov V, Vercauteren N, Barry C, Parlange MB (2012) The effect of scale on the applicability of Taylor's frozen turbulence hypothesis in the atmospheric boundary layer. *Boundary-Layer Meteorol* 143(2):379–391
- Horst TW, Kleissl J, Lenschow DH, Meneveau C, Moeng CH, Parlange MB, Sullivan PP, Weil JC (2004) Hats: Field observations to obtain spatially filtered turbulence fields from crosswind arrays of sonic anemometers in the atmospheric surface layer. *J Atmos Sci* 61(13):1566–1581
- Hutchins N, Marusic I (2007) Evidence of very long meandering features in the logarithmic region of turbulent boundary layers. *J Fluid Mech* 579:1–28
- Jensen N, Kristensen L (1979) Lateral coherence in isotropic turbulence and in the natural wind. *Boundary-Layer Meteorol* 17(3):353–373
- Kristensen L, Kirkegaard P (1986) Sampling problems with spectral coherence. No. 526 in Denmark. Forskningscenter Risoe. Risoe-R, Risø National Laboratory
- Kristensen L, Panofsky HA, Smith SD (1981) Lateral coherence of longitudinal wind components in strong winds. *Boundary-Layer Meteorol* 21(2):199–205
- Lenschow DH, Stankov BB (1986) Length scales in the convective boundary layer. *J Atmos Sci* 43(12):1198–1209
- Lumley JL, Panofsky HA (1964) The structure of atmospheric turbulence, monographs and texts in physics and astronomy, vol XII. Wiley
- Mann J (1994) The spatial structure of neutral atmospheric surface-layer turbulence. *J Fluid Mech* 273:141–168
- Mauder M, Zeeman MJ (2018) Field intercomparison of prevailing sonic anemometers. *Atmos Measure Tech* 11(1):249–263
- Midjjiyawa Z, Cheynet E, Reuder J, ágústsson H, Kvamsdal T, (2021) Potential and challenges of wind measurements using met-masts in complex topography for bridge design: Part II - spectral flow characteristics. *J Wind Eng Ind Aerodyn* 211(104):585
- Mizuno T, Panofsky HA (1975) The validity of Taylor's hypothesis in the atmospheric surface layer. *Boundary-Layer Meteorol* 9(4):375–380
- Mohan M (1998) Analysis of various schemes for the estimation of atmospheric stability classification. *Atmos Environ* 32(21):3775–3781
- Moré JJ (1978) The Levenberg–Marquardt algorithm: implementation and theory. In: Watson GA (ed) *Numerical Anal.* Springer, Heidelberg, pp 105–116
- Neumann PP, Bartholmai M (2015) Real-time wind estimation on a micro unmanned aerial vehicle using its inertial measurement unit. *Sens Actuators A* 235:300–310

- Panofsky HA (1962) Scale analysis of atmospheric turbulence at 2 m. *Q J R Meteorol Soc* 88(375):57–69
- Panofsky HA, Mizuno T (1975) Horizontal coherence and Pasquill's beta. *Boundary-Layer Meteorol* 9(3):247–256
- Pielke RA, Panofsky HA (1970) Turbulence characteristics along several towers. *Boundary-Layer Meteorol* 1(2):115–130
- Platis A, Siedersleben S, Bange J (2018) First in situ evidence of wakes in the far field behind offshore wind farms. *Sci Rep* 8(2163)
- Pope SB (2000) *Turbulent flows*. Cambridge University Press, Cambridge
- Rajewski DA et al (2013) Crop Wind Energy Experiment (CWEX): Observations of Surface-Layer, Boundary Layer, and Mesoscale Interactions with a Wind Farm. *Bull Am Meteor Soc* 94(5):655–672
- Ropelewski CF, Tennekes H, Panofsky HA (1973) Horizontal coherence of wind fluctuations. *Boundary-Layer Meteorol* 5:353–363
- Salesky ST, Anderson W (2018) Buoyancy effects on large-scale motions in convective atmospheric boundary layers: implications for modulation of near-wall processes. *J Fluid Mech* 856:135–168
- Salesky ST, Anderson W (2019) Revisiting inclination of large-scale motions in unstably stratified channel flow. *J Fluid Mech* 884
- Saranyasoontorn K, Manuel L, Veers PS (2004) A Comparison of Standard Coherence Models for Inflow Turbulence With Estimates from Field Measurements. *J SolEnergy Eng* 126(4):1069–1082
- Schlez W, Infield D (1998) Horizontal, two point coherence for separations greater than the measurement height. *Boundary-Layer Meteorol* 87:459–480
- Schlipf D, Trabucchi D, Bischoff O, Hofsäss M, Mann J, Mikkelsen T, Rettenmeier A, Trujillo J, Kühn M (2010) Testing of frozen turbulence hypothesis for wind turbine applications with a scanning lidar system. In: *Detailed Program, ISARS*. <http://www.isars2010.uvsq.fr/>
- Shimura T, Inoue M, Tsujimoto H, Sasaki K, Iguchi M (2018) Estimation of wind vector profile using a hexarotor unmanned aerial vehicle and its application to meteorological observation up to 1000 m above surface. *J Atmos Oceanic Tech* 35(8):1621–1631
- Shiotani M, Iwatani Y (1980) Gust structures over flat terrains and their modification by a barrier. In: *Wind engineering*. Elsevier, pp 203–214
- Simley E, Pao LY (2015) A longitudinal spatial coherence model for wind evolution based on large-eddy simulation. In: *2015 American Control Conference (ACC)*, pp 3708–3714
- Smalikho I, Köpp F, Rahm S (2005) Measurement of atmospheric turbulence by 2- $\mu$ m doppler lidar. *J Atmos Oceanic Tech* 22(11):1733–1747
- Stull R (2016) *Practical meteorology: an algebra-based survey of atmospheric science*. University of British Columbia, AVP International
- Taylor GI (1938) The spectrum of turbulence. *Proc R Soc Lond Ser* 164(919):476–490
- Thresher R, Holley W, Smith C, Jafarey N, Lin S (1981) Modeling the response of wind turbines to atmospheric turbulence. Oregon State Univ., Corvallis (USA). Dept. of Mechanical Engineering, Tech rep
- von Kármán T (1948) Progress in the statistical theory of turbulence. *Proc Natl Acad Sci* 34(11):530–539
- Wetz T, Wildmann N (2022) Spatially distributed and simultaneous wind measurements with a fleet of small quadrotor UAS. *J Phys: Conf Ser* 2265(2):022086
- Wetz T, Wildmann N, Beyrich F (2021) Distributed wind measurements with multiple quadrotor unmanned aerial vehicles in the atmospheric boundary layer. *Atmos Measure Tech* 14(5):3795–3814
- Wildmann N (2022) Multicopter UAS measurements at GM Falkenberg during FESSTVaL 2021. <https://doi.org/10.25592/UHHFDM.10148>
- Wildmann N, Wetz T (2022) Towards vertical wind and turbulent flux estimation with multicopter UAS. *EGU sphere* 2022:1–20
- Wildmann N, Rau GA, Bange J (2015) Observations of the early morning boundary-layer transition with small remotely-piloted aircraft. *Boundary-Layer Meteorol* 157(3):345–373
- Wildmann N, Päschke E, Roiger A, Mallau C (2020) Towards improved turbulence estimation with doppler wind lidar velocity-azimuth display (VAD) scans. *Atmos Measure Tech* 13(8):4141–4158